ISSN: 2997-6170

Research Article

Space Science Journal

Mesoscale and Large-Eddy Simulation of the Boundary Layer Process of Cumulus Development over Naqu, Tibetan Plateau Part A: Comparison Between Simulation and Observation

B. Kpaikpai[1, 3, 5], J. Sun[1,2*], J. Zhu[2,3], M. Banna[4], F. K. Ogou[6], F. Vuguziga[7] and D. Ntwali[8]

[1]*Key Laboratory of Cloud-Precipitation Physics and Severe Storms (LACS), Institute of Atmospheric Physics (IAP), Chinese Academy of Sciences (CAS), 100029, Beijing, China, emilkpaikpai@yahoo.fr, jimings@mail.iap.ac.cn, jzhu@mail.iap.ac.cn*

[2]*Key Laboratory of Geophysical Fluid Dynamics, IAP, CAS, jzhu@mail.iap.ac.cn, emilkpaikpai@yahoo.fr*

[3]*University of Chinese Academy of Sciences (UCAS), 100864, Beijing, China, emilkpaikpai@yahoo.fr, jzhu@mail.iap.ac.cn*

[4]*Laboratory of Physics, Energy, Thermal and Mass Transfers, Department of Physics, University of Lome, 01 BP 1515, Lome – Togo, magbanna@yahoo.fr*

[5]*Laboratory of Ocean and Atmosphere Interaction, Department of Physics and technology, University of Kara, P.O.Box: 404 Kara-Togo, emilkpaikpai@yahoo.fr*

[6]*Laboratory of Atmospheric Physics, Department of Physics, University of Abomey-Calavi, Cotonou 01 BP 526, Benin, ogofaustin@gmail.com*

[7]*Key Laboratory of Meteorological Disaster of Ministry of Education (KLME), Collaborative Innovation Center on Forecast and Evaluation of Meteorological Disasters (CIC-FEMD), Nanjing University of Information Science and Technology, Nanjing 210044, China, vfloribert@nuist.edu.cn*

[8]*Earth and Space Science, Rwanda Space Agency. drdidierntwali@yahoo.com*

[*]Corresponding Author
Jiming Sun, Key Laboratory of Cloud-Precipitation Physics and Severe Storms (LACS), Institute of Atmospheric Physics (IAP), Chinese Academy of Sciences (CAS), 100029, Beijing, China and Key Laboratory of Geophysical Fluid Dynamics, IAP, CAS, China

Submitted: 2024, May 01 **Accepted:** 2024, May 27 **Published:** 2024, May 31

Citation: Kpaikpai, B., Sun, J., Zhu, J., Banna, M., Ogou, F. K., et al. (2024). Mesoscale and Large-Eddy Simulation of the Boundary Layer Process of Cumulus Development over Naqu, Tibetan Plateau Part A: Comparison Between Simulation and Observation. *Space Sci J, 1*(2), 01-18.

Key Points

- The application of the WRF-LES model to reproduce the atmospheric boundary-layer processes of cumulus development over complex orography;
- Simulation of the ABL using observation nudging and comparison with TIPEX-III data and simulation data without Observation Nudging;
- WRF-LES simulations with observation nudging strategy better replicated the observed could pattern.

Abstract

Cumulus clouds are of great interest in numerical weather prediction. However, the scarcity of observed data on the Tibetan Plateau (TP) has not allowed a correct interpretation of their development. The Third TP Atmospheric Science Experiment provided experimental data to address this challenge. The objective of this study was to ascertain the effective utilization of observation-nudging techniques for the implementation of combined weather research and forecasting large-eddy simulation (WRF-LES) for further experimental designs. This study simulated cumulus clouds over southern TP on July 19, 2014, using the WRF-LES model and final reanalysis data from the Global Forecast System. We applied observation nudging and one-way nesting strategies to influence the optimality of WRF-LES runs. The study performed simulations with six different scenarios in comparison with observational data. The findings demonstrated that, despite being locally initiated and growing upscale, cumulus clouds were nonetheless subject to large-scale forcing. Simulations with observation nudging produced more accurate and trustworthy results than simulations without nudging when

compared to observations. While the observed time series were misleading, LES with mesoscale forcing produced a microphysical evolution that was consistent with the observations and an accurate water vapor profile. Without mesoscale forcing, LES provided the best ABL water vapor and sensible heat flux; however, it failed to provide a good microphysics field. In this aspect, large-scale forcing played an important role in cumulus development during the model experiment. The study recommended focusing on the model's response to the boundary conditions to improve the application of one-way nesting in separate iterations and observational nudging techniques.

1. Introduction

Small-scale unresolved motions in the atmospheric boundary layer (ABL) of Cumulus Cloud (CC) development have a major impact on larger-scale resolved signals. Numerical weather prediction (NWP) takes these procedures into specific account [1,2]. To strengthen the phenomenological foundation for meso- and micro-scale modeling (MMM), the physics of the ABL processes of CC development over complex terrains are actively being solved [3-5]. However, the latter modeling approach has several additional difficulties despite an increase in computing power, such as a lack of observation data over complex orography to replicate the CC development mechanism. MMM is ultimately limited by the availability of suitable boundary conditions to reproduce the evolution of the ABL processes [6]. The purpose of this work is to increase the coupled WRF-LES's applicability.

The Tibetan Plateau (TP), also known as "the third pole ", and "the water tower of Asia", is the world's largest and tallest plateau, located at coordinates 26°00′12 "N-39°46′50" N, 73°1′52 "E-104°46′59" E. Human life and the ecosystem of South East Asia (SEA) depend on water from the major rivers such as the Brahmaputra, Ganges, Irrawaddy, Mekong, Salween, Yangtze, and Yellow River, which headwaters are located on TP [7-11]. The water supply in these rivers is strongly related to the ABL processes of the cumulus convection that further produces precipitation fall [12]. In addition, the ABL processes over TP are well known to hydrating the global atmosphere [13-14]. However, the predictability of the latter process on TP relied on sparse and scarce observations that did not provide the required accuracy, spatial density, and temporal frequency, posing difficult challenges when applying numerical modeling to understand the CC development in that region [15]. The latest campaign work, the Third TP Atmospheric Science Experiment (TIPEX-III), conducted from July 1 to August 31, 2014, provided comprehensive experimental data, which motivated our interest in studying ABL process of CC development over Naqu in south TP (STP) [16,17].

CCs are typically detached and dense, with sharp outlines. They develop vertically in the form of rising towers. CCs often start to form in sunny and fair weather as soon as the rising air cools to the point where vapor becomes supersaturated. Subsequently, the water vapor condenses into liquid water droplets or solid ice crystals. Congestus CCs may develop into cumulonimbus clouds and generate thunderstorms when influenced by mesoscale instability, humidity, and temperature gradient. Cumulonimbus clouds grow vertically and may reach heights ranging from 300 to 12,000 m above ground level (AGL) [18]. The large CCs and thunderstorms are classified into meso-γ atmospheric processes [18-21]. CCs are precursors of other cloud types, while meteorologists may refer to CCs underway to determine the kind of weather that will occur. However, the ABL processes of CC developments have limited predictability due to uncertainty associated with the initial conditions. According to the Fifth Assessment Report of the Intergovernmental Panel on Climate Change [15], the numerical representation of the ABL clouds is an open problem in cloud modeling. This points out a need for the numerical study of ABL clouds development.

The broad classes of mesoscale phenomena influencing the ABL processes of CC development are the internally and externally forced-mesoscale processes. The former class derives structure and circulation within the atmosphere. The latter class results from the earth's surface-atmosphere interaction, including either thermal forcing due to the differential heating of the coupled earth's surface-atmosphere, or mechanical forcing due to the atmospheric response to the irregular topography [22-24]. Each area of TP, including south TP (STP), has particular ABL processes of CC development, interacting with large-scale forcing. The diurnal surface heating over TP in summer reflects an external forcing element, which interacts with a large-scale forcing, and mesoscale moisture transport then influences the ABL process of cumulus development. There is fifty years back, Flohn [25] highlighted that during the summer the TP act as a heat engine with an enormous convective chimney in the southeastern sector where giant cumulonimbus cells play a major role in continuously carrying heat upward into the high troposphere. Li et al. [26] and Ding et al. [27] revealed that warm and wet events have notably increased over the region and altered hydrological processes. As a result, various weather conditions influence billions of people living in the SEA region, particularly in the downstream sector [23,28,29].

The effect of the diurnal temperature variation on TP has been observed in the diurnal evolution of the TP's ABL structure, the most characteristic in the world. In dry and warm land surface-atmosphere conditions, the top of the ABL over TP could reach approximately 5 km of mean height AGL, higher than any reported ABL worldwide while a shallow ABL top is observed only about 2 km mean of height AGL in the moist condition of the coupled land-atmosphere system [13,30-35]. According to previous studies, ABL on TP exerts a profound thermal and dynamic influence on the cumulus development [28,32,33,36]. Many studies showed that the radiative budget of the ABL has a direct effect on the variation in CC cover [35,37,38]. However, the upper-level potential vorticity structures and the meridional position of the subtropical jet (STJ) also influence the feature of the ABL on the TP [32]. In midsummer, STJ and the South Asian High (SAH), interact and intensify the upper-level subsidence in STP's zones including the Naqu area, characterized by less cumulus development [30,32]. The mean position of the STJ was 40° north between 1979 and 2003 [30].

From the 1970s to 2014, three scientific experiments, including TIPEX-III, promoted the understanding of the cloud processes on TP [12,13,17,39]. However, the pursuit of in-depth knowledge of water and energy cycles on TP still raises questions related to multi-scale CC interactions. Three decades ago, Tingyang and Reiter [40] found that the condensation rate of water vapor in clouds, the clouds' liquid water content (LWC), and the precipitation efficiency in clouds are lower than those in surrounding regions through observation analysis and model simulations. Based on CloudSat and Cloud-Aerosol Lidar and Infrared Pathfinder Satellite Observations (CALIPSO), [41] further showed that CC convections were shallower over TP than those over the other two subregions of the TP–South Asian monsoon region. By contrast, the TIPEX-III campaign work revealed that most congestus CCs developed on TP, preferably in the afternoon, some of which penetrated vertically as high as 16.5 km AGL [13-17].

Most studies mentioned above focused on model simulations of the large-scale and mesoscale cloud processes on TP (28,40,42–44). In line with this, Fu et al. [39]. reviewed the progress of land-atmosphere interactions on TP. The authors suggested conducting an observational analysis coupled with numerical simulations to further understand the effect of ABL processes. Couvreux et al.[44]. pointed out that ABL water vapor variability is the main trigger of mesoscale convective clouds. Accordingly, this study analyzed the ABL features that may influence CC development.

Because of the extensive limitations in understanding the cloud processes on TP, Gao et al. [43]. showed that clouds and precipitation over TP have not been studied sufficiently due to the lack of observations over the harsh mountainous areas and the poor representation, in NWP models, of the CC processes over TP. Many studies emphasized that many modeling studies of CC processes on TP were probably inadequate to capture the complex interactions of the physical processes (17,43,45,46). Sato [32]. investigated the resolution dependency of the diurnal cycle of convective clouds on TP in a mesoscale model. They pointed out that convective clouds over TP during the day tend to have a small horizontal scale rather than a resolvable mesoscale resolution, and suggested further study with finer resolutions of less than 7 km. However, they did not specify how fine is enough to resolve the inaccuracy associated with the orography feature. With advances in the application of the coupled WRF–large eddy simulation (WRF-LES), it is now easy to understand the link between multi-scale CC development and determine the dominant trigger of CCs [47-49].

The objective was to determine the optimal applicability of the WRF-LES through an observation nudging technique for future experimental design. During the model experiment, the satellite images from Fengyun 2D showed an anticyclone over TP and evident cumulus in the surrounding area, Laser data reviled a very turbulent ABL, which motivated this work. To this end, this study organized the other steps as follows: Section 2 describes the experimental data and modeling framework. Section 3 gives a comparison between the simulation and observation. The summary and conclusions are presented in Section 4.

2. Data, Modeling Framework

2.1 Experimental Data

The study used the TIPEX-III dataset from 8 meteorological stations, where the surface measurements and L-band radiosonde soundings were used as input for the observation nudging to improve the initial and lateral boundary conditions (LBCs) and gradually adjust the model state toward observations during its integration. The purpose was to link the model's prognostic variables to the observed quantities to capture the atmospheric flow around the Naqu area, including Naqu1 and Naqu2. We can approximate the distance between Naqu1 and Naqu2 stations as 5.4 km. The stations consist of active remote sensing sites, automatic meteorological towers, ABL towers, and 2 surface weather observation stations, Naqu Plateau Cold Climate and Environment 1 and 2 (NPCE1 and NPCE2). These stations follow the recommendations of WMO, and all data from TIPEX-III are quality controlled before publication. The measurement devices used during TIPEX-III included operational radiosondes, cloud radars, laser ceilometer 31 (CL31), and other in situ observation devices. The Cold and Arid Regions Environmental and Engineering (CARE) research institute and the Chinese Academy of Sciences (CAS) support these stations in providing unique observation data. The data are distributed by the China Meteorological Administration (CMA). Describes most devices used during the TIPEX-III.

Station Name	Longitude (°E)	Latitude (°N)	Station Height (m) AGL	Station ID
LHASA*	91.133	29.667	3649	55591
LINZHI*	94.340	29.667	2992	56312
NAQU1*	92.067	31.483	4508	55299
NAQU2**	92.01	31.48	4507	55299
NPCE1	91.900	31.300	4534	-
NPCE2	90.900	31.300	4508	-
RIKAZE*	87.080	28.633	4302	55664
YITUOHE*	92.433	34.210	4534	56004

Table 1: Experimental data stations; asterisks indicate sounding sites; double asterisks indicate the source of radar reflectivity; AGL, above ground level

2.1.1. Surface and Tower-Based Measurements

Surface measurements from NPCE1 and NPCE2 and tower-based measurements from Naqu1 include air temperature (T_a), relative humidity (RH), air pressure (P), vapor pressure (e), and wind speed (U) [17,50]. We can decompose U into zonal (u) and meridional (v) wind as given in Equations (1) and (2) [51,52]. Tower-based measurements were available at 0.75, 1.5, 3, 6, 12, and 22 m height AGL. Data from each site were time series recorded from July 17 to 20, 2014. Each item in the series represents the mean of the data recorded over a 30-min period. The observed variable includes the mean wind speed U_z. The potential temperature difference $\Delta\theta = \theta(T_{az}) - \theta(T_{as})$, and specific humidity difference $\Delta q = q_s - q_z$, are unobserved and estimated from observed values and where subscript s represents 0.75 m height AGL and z represents 3 m height AGL for temperature and specific humidity, and 12 m height AGL for the mean wind speed. We can use the bulk transfer coefficient to estimate the HFX from wind speed and temperature data as given in Equation (3) [53-57]. Based on the latter studies, this study further estimated the latent heat flux (LH) as given in Equations (4) [54,55,58].

$$u = -U \cdot sin(\frac{\pi}{180} \cdot \varphi) \quad (1)$$

$$v = U \cdot cos(\frac{\pi}{180} \cdot \varphi) \quad (2)$$

$$\mathrm{HFX} = \mathrm{C}_p \cdot \rho_a \cdot \overline{\omega' \mathrm{T}'} \approx \mathrm{C}_p \cdot \rho_a \cdot \mathrm{C}_H \cdot \mathrm{U}_z \cdot \Delta\theta \quad (3)$$

$$\mathrm{LH} = \mathrm{L}_v \cdot \overline{\omega' \rho_v'} \approx \mathrm{L}_v \cdot \rho_v \cdot \mathrm{C}_E \cdot \mathrm{U}_z \cdot \Delta q \quad (4)$$

Where φ is the wind direction, L_v=2.501–(2.361. 10^{-3})·T is the latent heat of vaporization, C_p is the specific heat of the air, ρ_a is the mean air density, and C_H and C_E are the bulk transfer coefficients for heat (Stanton number) and moisture (Dalton number), respectively [60]. In this study, $\overline{w'T'}$ and $\overline{w'\rho_v'}$ represent the kinetic surface flux of heat and moisture, respectively. The variable w represents the vertical wind speed, while the prime indicates fluctuations around the mean value. The overbar denotes time averaging on the 30 minutes basis. The estimation was done assuming the bulk transfer coefficients equal to the drag coefficient (C_D). As calculated by the previous study, the drag coefficient was found to be C_D=4.4·10^{-3} [60,61] for the Naqu area, and there was no need to perform this calculation in this study.

2.1.2. L-Band Radiosonde Sounding Measurements

The L-band radiosonde sounding stations are indicated with an asterisk in Table 1. The variables used in this study include air temperature, wind speed, wind azimuth, air pressure, relative humidity, and geographical height. The data were recorded each minute for about 1.5 hours and were available at the predetermined synoptic times, except on July 18, 2014, where 3 soundings were launched, at 0615UTC, 1115UTC, and 2315UTC, over Naqu1. Wind speed and azimuth were used to decouple the wind field into meridional and zonal wind components. The latter was used as input for observation nudging.

2.1.3. Automatic Laser Ceilometer Measurements

The ABL height data were determined over Naqu2 with a Vaisala CL31 automatic laser ceilometer. The CL31 has a time resolution of 16 s and a vertical resolution of 5 m. The CL31 used in this study is a mini-Lidar made in Finland and maintained by China Ocean University. The CL31 is used for active remote sensing measurements to characterize the ABL height with the backscatter signal and has good accuracy [61,62]. This study used the measurements from the CL31 as a reference for the simulated ABL. The purpose of using the CL31 measurement was to avoid a false ABL depth estimation.

2.1.4. Ka-Band Millimeter-Wave Radar and Fengyun 2D Satellite Images

The cloud data were performed over Naqu2 using a Ka-band millimeter-wave cloud radar. The radar produced the cloud data at a time resolution of 0.85 s and a vertical resolution of 30 m. The data from July 19, 2014, were used to retrieve the radar reflectivity. The radar reflectivity mentioned here is a measure of the fraction of the precipitation intensity reflected from the cloud surface. The millimeter-wave cloud radar data browsing software, HMB-Disp, provided by Naqu2 was used to extract the radar reflectivity. Visible light 2D images from the Fengyun (FY-2D) geostationary meteorological satellite at 16:45 local standard time (LST) on July 19, 2014, were also used as a reference to simulated reflectivity. The original data has a horizontal resolution of 5600 × 4800 pixels.

2.2 WRF Modeling Framework

2.2.1. WRF Model Description

The WRF model is a non-hydrostatic, compressible atmospheric model, which is the most widely used in NWP for research and operational needs [63]. The WRF model has grid nesting capability, which allows simultaneous multiscale simulation [64]. The model has several initialization programs for idealized and real-data simulation cases and provides several parameterization options, such as land surface, surface layer, planetary boundary layer (PBL), microphysics, CC parameterization, and adaptive

subgrid-scale (SGS) mixing parameterization [65-67]. In this model, the turbulent kinetic energy and non-local closure schemes enable the PBL to develop with entrainment [68,69].

As mentioned above, the WRF model has more computing power and allows the coupled WRF-LES to perform real-time simulations at meso- and micro-scales resolutions [16,72]. The purpose of applying the LES is to implicitly calculate the small-scale turbulence from the flow field and explicitly resolve the largest scales of energy production, while the basis of the LES strategy in the WRF model is low-pass filtering [48,71,73,74]. The application of coupled WRF-LES in real-time simulation mode uses a surface layer scheme to connect the lower boundary and the atmosphere.

Mesoscale Simulation Runs				
Simulation Type	$\Delta x_{i=1-5} = \Delta y_{i=1-5}$ (m)	Horizontal Grids Points	$\mathcal{A}$ (km^2)	∂t(s)
$D0_{i=1}$ Mesoscale$-\gamma$	9,234	150 × 150	1385.1 × 1385.1	15
$D0_{i=2}$ Mesoscale$-\gamma$	3,078	150 × 150	461.7 × 461.7	5
$D0_{i=3}$ Microscale$-\alpha$	1,026	150 × 150	153.9 × 153.9	5/3
Large-Eddy Simulation Runs				
$D0_{i=4}$ Microscale$-\alpha$	342	150 × 150	51.3 × 51.3	3/20
$D0_{i=5}$ Microscale$-\beta$	114	150 × 150	17.1 × 17.1	1/20

Table 2: Five nesting domains, $\Delta x_{i=1-5} = \Delta y_{i=1-5}$, represent grid spacing (m) where i ranges from 1 to 5 to represent the domains $D0_{i=1}$, $D0_{i=2}$, $D0_{i=3}$, $D0_{i=4}$, and $D0_{i=5}$); $\partial t(s)$, the time step in seconds; A is the area of the domain (km2).

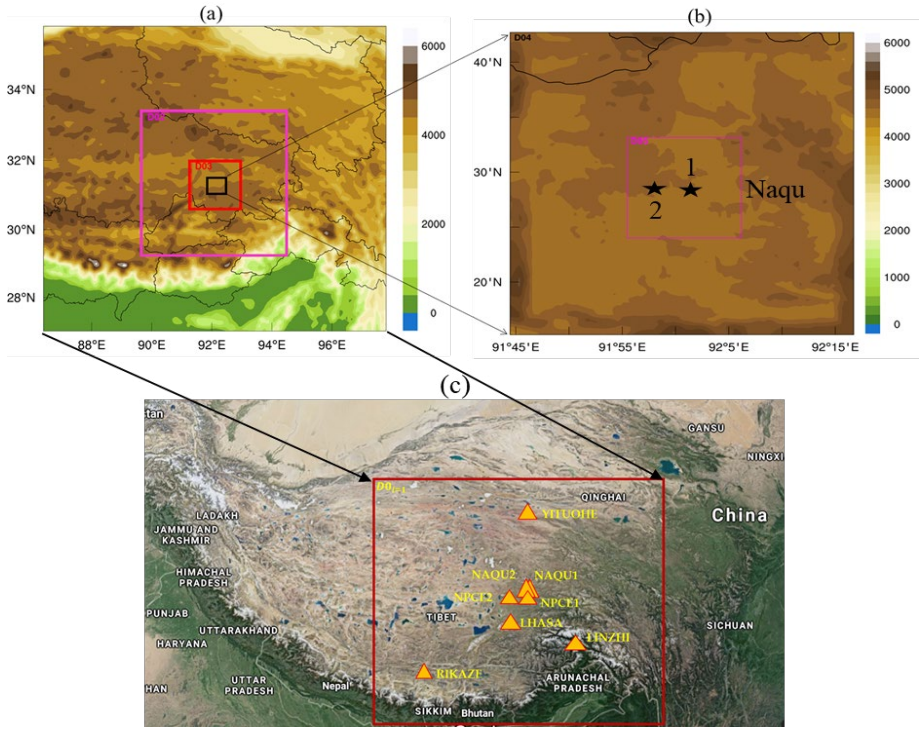

Figure 1: WRF domain configuration: (a) mesoscale domains, (b) microscale domains; shaded area represents terrain height (m) above sea level (ASL). The black stars 1 and 2 are respectively the Naqu1 and Naqu 2 stations (c) google map with yellow triangles indicating the location of each station.

The coupled WRF-LES is constructed by applying a one-way nesting strategy in two separate iterations. This strategy is an option in the WRF model, defined as a finer-grid-resolution run. This strategy is used as a subsequent run after the coarser-grid-resolution run, where the program (ndown) is run in between the two simulations. The coarse-grid run provides the initial and lateral boundary conditions (LBCs) to the finer-grid run, with data from higher-resolution land and masked surface fields. The latter strategy only feeds suitable information from the outer domain to the inner one. The one-way nesting strategy has been used in many studies with good results [75,76].

Sariano et al. (76) suggested that for mesoscale simulation runs, the one-way nesting technique should be used because two-way nesting gave the worst results in their case study. Zhu et al. (49) suggested that using one-way nesting runs allows simulation of complicated and heterogeneous forgings, and recommended that this strategy be used for cloud cases that require extremely high resolution.

The WRF model system also includes the observation nudging strategy used in this study. This strategy uses Newtonian relaxation to improve either the dynamics initialization or analysis, respectively [77]. However, assimilation of moisture fluxes may pose particular difficulties when applying observation nudging due to the high spatial variability of the variables such as the water vapor mixing ratio and specific humidity relative to their absolute values [78]. For simplicity, this study applied observation nudging to wind and temperature to avoid excessive drying that can be caused by negative water vapor values occurring within the model domain.

2.2.2. WRF Model Domain Configuration

This study used version 3.8 of the WRF-ARW dynamical solver installed on the Tianhe high-performance computing (HPC) system and assisted by the Sugon HPC system from the State Key Laboratory of Disaster Prevention and Reduction for Power Grid Transmission and Distribution Equipment (SKL) at Changsha, China. To get a suitable design for the multiscale atmospheric reanalysis, we designed 5 WRF model domains, $D0_{i=1\text{-}5}$, where $D0_{i=1} = D01$, $D0_{i=2} = D02$, …, $D0_{i=5} = D05$ by assigning $D0_{i=1\text{-}3}$ to mesoscale simulations, and 2 microscale domains $D0_{i=4,5}$ all in $D0_{i=3}$, assigned to LES runs. The model domain configuration is given in Table 2 and depicted in Figure 1. As shown in Figure 1a, Naqu1 is the center of all domains. The parent domain $D0_{i=1}$ includes China's 6 administrative prefectures, Naqu, Linzhi, Lhasa, Rikaze, Shannan, Chamdo, and Yituohe, and neighboring southern countries. As shown in Figure 1b, $D_{0\ i=4}$ was configurated to cover Naqu1 and Naqu2 observation stations, while Naqu1 is the center of $D0_{i=5}$.

As shown in Table 2, each domain has 150 horizontal grids. In this configuration, the innermost domain has 114m horizontal grid resolution with an area of 114×114 km^2 including Naqu1 and Naqu2. In this configuration, some vertical layers were set to 50 full sigma levels up to 50 hPa, except in one scenario namely scenario B1 where the vertical levels have been increased and reorganized manually to be many within the ABL. In the domain configuration for scenario B1, the vertical layers are composed of 56 full sigma levels up to 50 hPa, while the vertical increment Δz_i=0-55) between two consecutive levels increased linearly following the hyperbolic cosine function:

$$\left\{\Delta z_i = Ch(\lambda_i) = \frac{e^{\lambda_i} + e^{-\lambda_i}}{2};\ \lambda_{i=0-55} \in [2.797324366;\ 8.217039]\right\}$$

In the latter configuration, the first model level's height is 8 m AGL, while the first 40 model levels are below 4000 m height AGL (~300hPa). The domain $D0_{i=3}$ provides the initial conditions for $D0_{i=4}$ to optimize LES results. The horizontal and vertical interpolations are performed with an overlapping quadratic approach and linear log pressure, respectively. These interpolations allow the boundary forcing to vary in time and space. Mesoscale simulations use 1D PBL parameterization to fully parameterize the anisotropic turbulent motion using the Reynolds-averaged Navier–Stokes (RANS) technique, whereas LES runs treat unresolved isotropic turbulence using SGS schemes [79]. In fact, different ranges of scales from microscale to mesoscale must be solved to obtain a complete representation of the superimposed physical mechanisms involved in the ABL process of CC development. However, in the coupling model domain configuration, there is a range of grid resolutions where certain processes are neither sub-grid nor resolved, the so-called "grey zone" or "terra incognita". These domains may be considered either mesoscale using 1D PBL or microscale requiring LES strategy. Talbot et al. (72) successfully used $D0_{i=4}$= 450m for LES runs of the ABL. This study increased the resolution for $D0_{i=4}$, be closer to the LES standard.

Our study focused on ABL processes of CC development on July 19, 2014. However, all simulations were performed over 72 hours from July 17 to 20, 2014. This is because TP is at a very high altitude and has complex orography, which causes the model to be statically unstable. Therefore, after several text experiments, this study assumed that 24 hours are enough to assess the effect of the model's spin-up during model domain initialization. The history interval was set to 15 minutes to create high time resolution data. We recorded 48 hours series (from day 2 to day 3) for comparison with the observed data from TIPEX-III.

The traditional United States Geological Survey dataset (USGS) collected from 1992 to 1993 was applied to account for the influence of terrain and its related water bodies on WRF-LES surface heat fluxes and meteorological variables. This study selected USGS 30 arc-second (~900 m) Details on the data are given at the USGS website (http://www.usgs.gov/). Liu et al. (16) and Sertel et al. (80) demonstrate that the use of the default WRF dataset may cause misrepresentation of the study region, while, there are spectral mixing problems between classes in land use. Therefore, this study tested the high-resolution Shuttle Radar Topography Mission (SRTM) dataset, 3 arc-second (~90m) for comparison with USGS dataset (Not shown). The data can be downloaded at (http://www2.jpl.nasa.gov/srtm/). However, there needed to be no improvement with SRTM dataset. Some simulation results can be seen in Figure 1 of the supplementary file.

Initial and lateral boundary conditions were generated from the National Centers for Environmental Prediction (NCEP) Final Analysis (FNL) derived from the Global Forecast System (GFS) and were accessed on September 05, 2019. FNL data have a resolution of 1° x 1° grids at six-hourly time steps with 26 vertical levels from 10 to 1000hPa of isobaric surface data and can be downloaded at https://doi.org/10.5065/D6M043C6.

2.2.3. Flow Parameterization Options

This section gives details of the parameterization schemes used in this study and describes the experimental design. It also presents the one-way nesting strategy that coupled mesoscale simulations with microscale one. Table 3 summarizes the parameterization options. As shown in Table 3, the coupled land-atmosphere fluxes were computed using the Unified Noah Land Surface Model (82,83). Surface boundary conditions used Monin–Obukhov logarithmic similarity theory to prescribe fluxes of heat, moisture, and momentum (84–86). The Mellor–Yamada scheme (87) was selected for mesoscale simulations to account for turbulent kinetic energy (TKE) in local vertical mixing. The Thompson scheme was selected to parameterize the microphysical process. Short- and longwave radiation were integrated from the radiative transfer scheme (RRTMG) (88,89). Kain (90) (hereafter referred to as KF) proposed a deep and shallow CC convection scheme, which was selected to resolve CC processes only in domain $D0_{i=1}$. Jeworrek et al. (90) suggested combining the KF and Thompson microphysics schemes to improve the high-resolution numerical simulation results. However, the KF scheme was useless for $D0_{i=2\text{-}5}$, respectively, because these domains fell into the grey zone. On the other hand, a test simulation with the KF scheme in LES runs provided too much precipitation. Some pictures are shown in Figure 3 of the supplementary file.

Parameterization options	Mesoscale domains			Microscale domains	
	$D0_{i=1}$	$D0_{i=2}$	$D0_{i=3}$	$D0_{i=4}$	$D0_{i=5}$
Cumulus	Kain–Fritsch	Useless			
Planetary boundary layer	Mellor–Yamada			Real-time LES mode in periodic lateral boundary condition	
Surface layer	Monin–Obukhov				
Land-surface	Unified Noah LSM				
Cloud microphysics	Thompson				
SGS stress model	Useless			TKE1.5	

Table 3: Summary of flow parameterization. SGS, subgrid-scale; $D0_{i=1\text{-}5}$.

For the real-time LES in the high mountain range, the recommended SGS turbulence model is a 1.5-order of TKE energy (TKE1.5) closure model (65). The TKE1.5 model accounts for diffusive transport of the TKE and allows more uniform diffusivity and entrainment through the convective ABL (16,45,67,74). In real-time simulation LES mode, the use of SGS TKE1.5 needs a filter (C_k) in the inertial subrange to filter the SGS noise (47,80). The filter was set to a default value (C_k = 0.15) in this study. The advection options of order $O(h) = 5$ and $O(h) = 3$ were used to compensate for the coarser horizontal resolution (65).

2.2.4. Experimental Design

We designed six scenarios (case experiments A, B, B1, C, D, and E), based on Talbot et al. (72) and Heinze et al. (92), to account for the reliability of simulation results compared to observations, the efficiency of physical parameterization, and the skill of the strategy used in each scenario. These allowed us to prescribe dynamics associated with ABL process of CC development over TP. We first assessed the mesoscale simulations, then performed the LES runs through a one-way nesting strategy, as presented in Table 4.

Mesoscale Simulations	Case	Input Data	Horizontal Turbulence	Eta levels	Horizontal Grid Spacing $\Delta x_{i=1-3} = \Delta y_{i=1-3}$ and $R_{i=1-3}$		
					$D0_{i=1}$ $\Delta x1 = \Delta y1$ =9,234 m	$D0_{i=2}$ $\Delta x2 = \Delta y2$ = 3,078 m	$D0_{i=3}$ $\Delta x3 = \Delta y3$ = 1,026 m
	A	FNL	TKE1.5	50, 1rst model level: 65 m with 16 $layers$ $< 4000m$	R_1 is useless	R_2 is useless	R_3 is useless
	B	FNL, Obs.			R_1 = 980,000 m	R_2 = 330,000 m	R_3 = 120,000 m
	B1			56, 1rst model level: 8 m with 40 $layers$ $< 4000m$			
Microscale Simulations	Case	Input Data		Parent Mesoscale Turbulence Model	SGS Turbulence Model	Horizontal Grid Spacing $\Delta x_{i=4,5} = \Delta y_{i=4,5}$ and $R_{i=4,5}$	
						$D0_{i=4}$ $\Delta x4 = \Delta y4$ = 342 m	$D0_{i=5}$ $\Delta x5 = \Delta y5$ = 114 m
	C	Input from case B, FNL, and observation		TKE1.5	TKE1.5	R_4 = 40,000 m	R_5 = 15,000 m
	D	Observation and FNL		The parent mesoscale turbulence model (TKE1.5) is useless			
	E	FNL					

Table 4: Controlled experiment for mesoscale simulations and LES; observation data were used through Observation Nudging strategy; FNL, final reanalysis; TKE1.5, one and a half order turbulent kinetic energy closure model, used in anisotropic turbulence for mesoscale simulations and isotropic turbulence for LES; $R_{i=1-3}$ represent the radii of influence values from $D0_{i=1}$ to $D0_{i=3}$, and $R_{i=4,5}$ are the values from $D0_{i=4}$ to $D0_{i=5}$, Eta levels were generated automatically for cases A, B, and C but customized for case B1. SGS, subgrid-scale.

As presented in Table 4, we designed a mesoscale simulation, scenarios A as a benchmark experiment to help determine the optimality of observation nudging in scenario B. We applied observation nudging in scenarios B, B1, C, and D. The nudging strength in these simulations was set to $120\times e^{-4}\ s^{-1}$. As shown in Table 4, the radii of influence were set to $R_{i=1-5}$, respectively for $D0_{i=1-5}$). Each radius of influence on a given domain was slightly greater than a half-diagonal of that domain. Therefore, each point of the WRF domain at any distance within the domain will be influenced at least by one observation station. Observation stations are less dense and sparse (Figure 1c). We wanted every observation at any station to influence the whole domain at maximum. Therefore, scenario B determines the impact of observation nudging on the simulation results. Scenario B1 determines the optimality of the external forcing on the ABL such as surface drag and heating caused by the infrared radiation divergence imposed to the atmosphere. Note that surface characteristics directly affect ABL. Therefore, increasing the layers in this part accentuates the effect of surface characteristics on the simulation results. Scenario C is an LES that determines the effect of large-scale forcing on microscale circulation. LES is useful for understanding the specific processes underlying the ABL, clouds, etc. In this scenario, a one-way nesting strategy was performed between $D0_{i=3}$) and $D0_{i=4}$ where the former provides the boundary condition for the latter with data from higher resolution land and masked surface fields. As mentioned earlier, this strategy only feeds suitable information from $D0_{i=3}$ to $D0_{i=4}$ and there is no feedback between these two domains. Scenario C differs from scenario D only by the use of the one-way nesting strategy. Indeed, scenario D is a control experiment for scenario C, which helps to determine the optimality of applying the one-way nesting strategy. We designed the scenario E as a benchmark experiment for LES run to help determine the optimality of observation nudging in scenario D. The vertical resolution has not been tested for scenarios C, D, and E due to their very high computational cost. Briefly, in this approach, we focused on scenario B to achieve our objective of using observation nudging. Scenario C utilized the input from scenario B as the boundary condition, and we were expecting the scenario C to reproduce the results from B but is much improved. Heinze et al. [92] the same approach to evaluate the mean ABL quantities and turbulence statistics.

2.2.5. Metrics for Comparison

The comparison between the simulated time series and observation is based on the mean bias (MB) and the root mean

squared error (RMSE) statistics (93,94) as given in Equations (12) and (13), respectively:

$$\mathbf{MB} = \frac{\sum_{j=1}^{n}(f_j - o_j)}{n} \quad (12)$$

where $f_{j=1,\ldots,n}$ are the simulated values from the model, $o_{j=1,\ldots,n}$ are the observation values, and n is the number of data points used in the calculation; and

$$\mathbf{RMSE} = \sqrt{\frac{\sum_{j=1}^{n}(f_j - o_j)^2}{n}} \quad (13)$$

Mean bias represents a gross measure of reliability, while RMSE represents a measure of the spread of differences between the forecast and observed values with the same units of measurement.

3. Comparisons Between Simulations and Observations

3.1. Comparison between simulated time series and observed

The comparison scores are shown in Table 5, and Figures 2a and 2d illustrates the time series used for model comparison. We considered the period after 24 hours of spin-up time for comparison, that is from day 2 to 3. Table 5 shows that WRF-LES had a general tendency to overestimate the observation field except for the temperature, where the model underestimated the observation in all scenarios.

Table 5 shows that scenario A has a more accurate result in temperature than those in other simulations. The lowest score value is 1.8 K for RMSE. The largest values found in scenario A are LH scores of 61.64 w/m^3 for MB and 72.21 w/m^3 for RMSE. Large LH indicates large precipitation. As shown in Table 5, scenario B overestimated the observation except for the temperature. However, it tended to record the best lowest score values for wind speed (0.16 m/s for MB and 1.05 m/s for RMSE) and LH (69.57 w/m^2 for RMSE). The release of LH plays a role in heating the air, which rises. The air cools while the water vapor condenses, gradually forming clouds. Therefore, scenario B should provide the best distribution of cloud patterns compared to observation.

The scenario C, as shown in Table 5 overpredicted the observation, with a tendency to record the largest score values, especially for WSD (4.89 m/s for MB, 5.94 m/s for RMSE) and LH (61.98 w/m^2 for MB and 111.44 w/m^2 for RMSE). As mentioned earlier, WRF-LES overestimated observation in LH and predicted excessive precipitation. From the visual inspection, unexpected high wind speed values in scenario C (Figure 2a) contributed to high LH. Thus, the overprediction of wind speed in scenario C may be related to lateral boundary noise in the WRF-LES model runs, specifically when using a one-way nesting strategy in separate iteration steps. In fact, the one-way nesting strategy in separate iterations for the wind speed simulation over unresolved topography may increase errors in simulation results.

As shown in Table 5, scenario D provided a more accurate result in HFX compared to other scenarios, with the lowest score value of 40 w/m^3. Also, scenario D had reliable results in temperature and LH, with the lowest score values of –0.16 K and 44.98 w/m^3, respectively. Referring to a study by, WRF-LES runs in scenario D can predict the best ABL because it has better results in HFX.

Score	Boundary-Layer Variables	Case A	Case B	Case B1	Case C	Case D	Case E
MB	Temp (K)	-0.41	-0.42	-0.15	-1.01	-0.16	2.02
	WSD (m/s)	0.83	0.07	1.32	4.75	4.56	3.80
	HFX (w/m^2)	42.24	37.88	19.26	-4.57	-23.87	-5.50
	LH (w/m^2)	61.64	56.26	97.41	-21.36	44.98	78.59
RMSE	Temp (K)	1.8	1.86	2.83	3.31	3.11	3.12
	WSD (m/s)	1.56	1.20	3.12	6.27	6.14	5.20
	HFX (w/m^2)	56.89	53.62	56.54	44.07	40.00	54.78
	LH (w/m^2)	72.21	69.57	132.71	103.20	89.45	116.00

Table 5: The mean bias (MB) and the root mean square error (RMSE) for two-meter temperature (T2), 10 m wind speed (WSD), the sensible heat flux (HFX), and the latent heat flux (LH); four scenarios are denoted as cases A, B, C, and D. $D0_{i=3}$ is the third domain and $D0_{i=5}$ is the fifth domain.

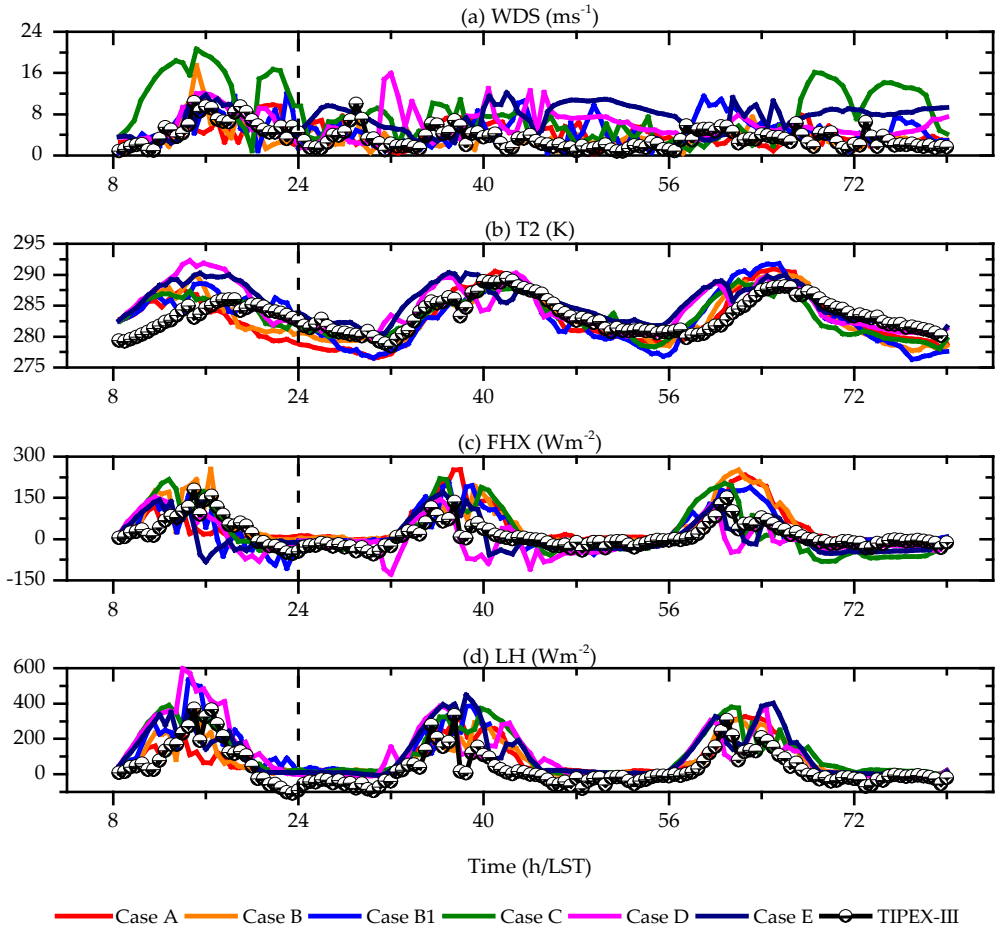

Figure 2: Time series of surface variables from $D0_{i=3}$ of the scenarios A, B and B1, and from $D0_{i=5}$ of the scenarios C, D and E (Table 4), compared to time series from Naqu1 (92.067, 31.483): (a) wind speed (WSD); (b) Two-meter temperature (T2); (c) the sensible heat flux (HFX) at the surface; (d) the latent heat flux (LH) at the surface. Dashed lines indicate the upper limit of spin-up time.

Overall, for surface meteorological variables and heat fluxes, considering the set of results in each scenario, scenarios B and D had more accurate and reliable results than scenarios A, B1, and C. However, compared to the scenario A we found that the observation nudging strategy improved WSD, FHX, and LH results in the scenario B and HFX results in the scenario C and D. In fact, some results from the scenario C such as MB relative to HFX and LH were least scores and have a relatively good RMSE. However, we believe that noise occurred while transitioning through the 'ndown' program during the performance of the one-way nesting strategy. This is because

3.2 The Simulated and Observed Boundary Layer Height

The ABL height is a fundamental parameter characterizing the depth of atmospheric mixing near the earth's surface. It is critical for understanding the cloud processes related to ABL features and their feedback on the weather and climate system. The detection of ABL height from Lidar is as follows: at the top of the ABL, water vapor decreases abruptly and affects the Lidar signal to change rapidly around the ABL top.

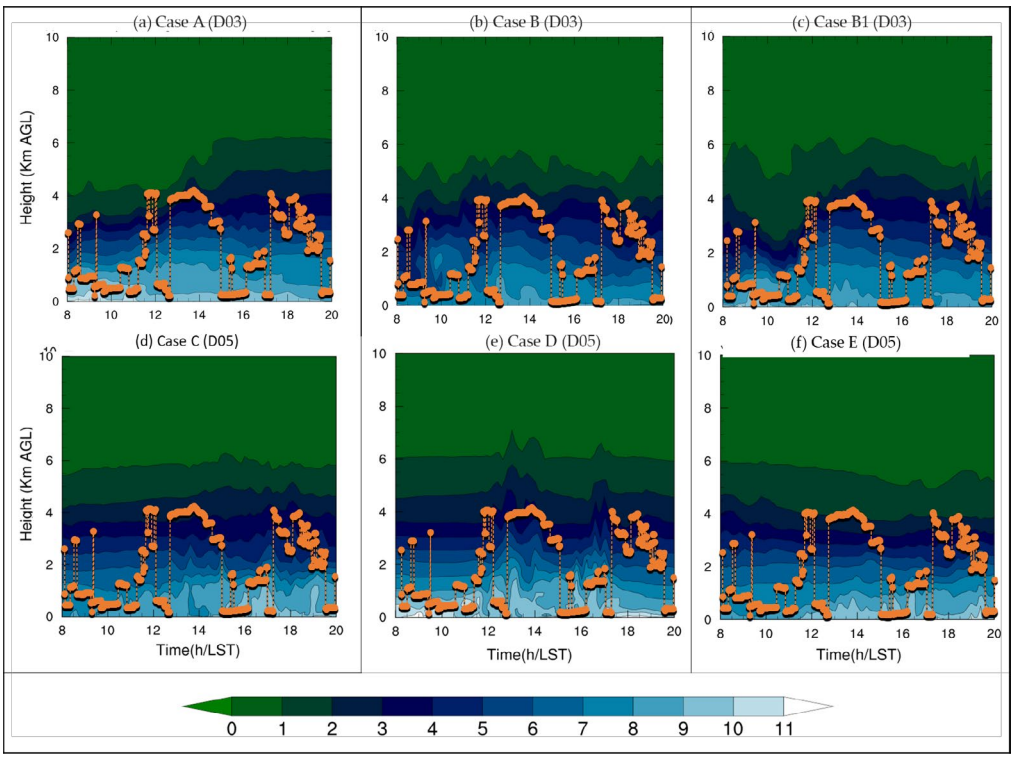

Figure 3: Time-high cross-section of water vapor mixing ratio (g/kg) (shaded) over Naqu1 predicted on July 19, 2014, at local standard time and compared to laser ceilometer measurements of the boundary layer height (ABL) from the Third Tibetan Plateau Atmospheric Science Experiment (TIPEX-III). Cases A, B and B_1 from $D0_{i=3}$) =$D03$, C, D and E from $D0_{i=5}$ = $D05$ represent scenarios in Table 4.

In this study, we compared the simulated ABL to that from the CL31 measurements based on the time–height cross-section of the water vapor mixing ratio. We found three peaks of the ABL from CL31 measurements, at 12:00, 14:00, and 18:00 LST. The peak found at 12:00 LST may be related to intermittent turbulence. The diurnal peak was reached around 14:00 LST. The peak found at 18:00 LST may have arisen from the high HFX released after intense convection developed in the early evening. We can also look for the last two peaks in the time series from temperature and heat fluxes shown in Figure 2 between the 56th and 72nd hours of the simulation period. The simulated ABL shows undulations and plumes of the water vapor mixing ratio with the mixing decreasing with height. We depicted the results of the comparison in Figure 3. Upon visual inspection, we can estimate the simulated ABL height as the height at which the water vapor mixing ratio is 4 g/kg. This is because the CL31 measurements fit better with that height in scenarios C and D (Figures 3d and 3e).

In the overall mesoscale simulation results, scenarios A, B, and B1 (Figures 3a, 3b and 3c) presented a convective ABL between 10:00 and 20:00 LST, slightly higher than the observed. We note that in dry and warm land surface-atmosphere conditions, the top of the ABL over TP is deep, while a shallow ABL characterizes the moist condition of the coupled system. Under current conditions, it is perceived that all mesoscale simulations will reproduce little clear skies with few cumulus clouds (examples: case B and B1 of Figures 5c and 5d, respectively). It has been noted that scenarios A, B, and B1 each effectively capture the diurnal peak of the Atmospheric Boundary Layer (ABL). However, the model's ability to replicate the ABL peak around 18:00 LST was found to be inadequate. This is probably related to the PBL scheme, which cannot treat the surface heterogeneity well. In scenarios C and D (Figures 3d and 3e), the ABL peaks collapsed slightly compared to the CL31 measurements, but the simulated ABL has a similar trend to CL31. The input from the mesoscale simulation forced LES from scenario C, which affected the simulated ABL structure. We can therefore consider that applying the one-way nesting strategy could increase the noise in the ABL structure due to complex topography that is not resolved in the scenario C. Particularly, in the scenario D (Figure 3d), the boundary between the free and moist atmospheric layers followed the trend of the CL31 measurement. Scenario E presented a relatively shallow ABL. According to our hypothesis, it is likely that scenario E will produce a cloudier sky. The ABL from each scenario, depending on its features, developed CC convection more or less consistent with the observed. To set this idea down, we discuss the convection that occurred between 16:00 and 20:00 LST in the next subsections.

3.3 Pattern Reflectivity and FY-2D Satellite Image

We compared the simulated reflectivity (Figures 4b and 4e) to the radar reflectivity from TIPEX-III performed over Naqu2 (Figure 4a). The maximum intensity of reflectivity in scenarios A and B1 was similar to the intensity (10 dBZ) of the observed reflectivity, whereas in scenarios B, C, D and E, the model overpredicted

the intensity of the observed reflectivity by 30 dBZ. We verified from the observation that very weak or almost no precipitation occurred over Naqu2 between 15:04 and 18:46 LST. By contrast, the model presented maximum reflectivity before 18:00 LST in all scenarios except scenario C. Comparing the numerical pattern reflectivity in each scenario to the observed, the model anticipated the observed reflectivity over Naqu2 by at least three hours, which can be seen in the time series of surface variables shown earlier in Figure 3. The reflectivity in scenario C reflects the observed better than in other scenarios. The reflectivity in scenarios D and E (Figures 4f and 4g) reached a height above that observed in scenario C (Figure 4d) with similar intensity. But the maximum precipitation (the orange shaded reflectivity) observed from TIPE-III (Figure 4a) around 19:00 LST at the Naqu site was rather predicted just after 16:00 LST. The little improvement relative to the prediction time of the precipitation intensity in scenario C may be related to the combination of the one-way nesting and observation nudging strategies. Note that scenarios D and E have not applied a one-way nesting strategy. On the other hand, the earlier comparison result showed that scenarios C, D and E overpredicted the surface wind speed and hence the latent heat flux and intense precipitation. Wind speed depends on the large-scale pressure gradient force and the local geography. In addition, as the wind speed is modulated by the large-scale forcing, it is obvious that scenarios D and E presented different results from scenario C because they performed LES without a one-way nesting strategy. Furthermore, the difference between scenario D and E is because scenario E has not used observation nudging strategy.

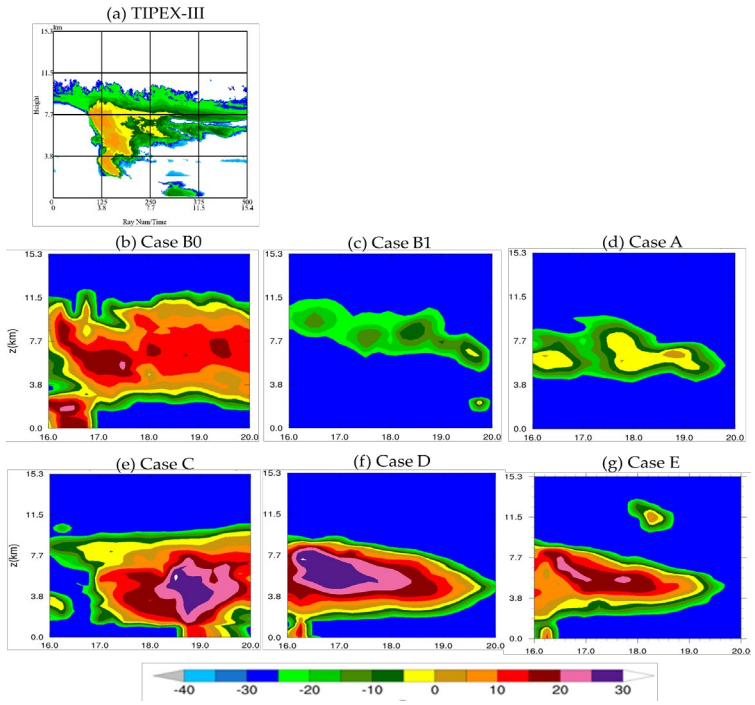

Figure 4: Vertical cross-section of pattern reflectivity on day 3 of simulation period: (a) the observed radar reflectivity from TIPEX-III between 18:45 and 20:00 LST on July 19, 2014; (b–e) simulated reflectivity. Cases A, B and B1 from $D0_{i=3} = D03$, C, D and E from $D0_{i=5}) = D05$ represent scenarios in Table 4.

3.4. Simulated Liquid Water Content and The Vertical Wind Shear

We investigated the types of cumulus clouds (CCs) and the effect of the vertical wind shear on their development in each scenario, based on the amount of the liquid water content (LWC). Vertical wind shear is a factor that determines the origin of clouds forming over a given region, while the amount of LWC in the atmosphere determines what types of clouds form. We illustrated the LWC in Figure 5 at 200, 300 and 400hPa levels, respectively, each overlapped with the vertical wind shear. Note that Fengyun's satellite images (Figures 5a and 5b) are plane projections including clouds from the low level to the tropopause. The white parts of Fengyun's satellite images represent the CCs. The dark parts of the images represent no clouds. We depict LWC and wind shear at 16:48 LST. This analysis emphasizes CC and cumulonimbus clouds development. Hess et al. [93-95]. classified the types of clouds associated with the amount of LWC over land and recommended 0.25 g/m^3 ≤ LWC ≤ 0.3 g/m^3 for CC and stratocumulus clouds, and 1 g/m^3 ≤ LWC ≤ 3 g/m^3 for cumulonimbus. Scenarios A and E were useless in this analysis due to their uncertainty with the observed clouds. Moreover, these scenarios were not the target scenarios so far.

In scenario, B, Figures 5c and 5d shows a spatial distribution of LWC similar to that of the cloud distribution in Fengyun's satellite image (Figure 5a). However, compared to the satellite image, scenario B shows scattered small CCs and some Cumulonimbus with LWC ≥ 1 g/m3 from the mid-level (Figure 5d) to the upper level (Figure 5e) at the northwest and southeast flanks, respectively. Scenario B also presents a strong vertical wind shear. As we can see in Figure 5c, there is a southwesterly low-level jet (LLJ) at 400hPa. The LLJ is a monsoonal wind

that provides moist air favorable for cloud formation. The southeasterly wind dominates the middle-level (300hPa). The upper-level (200hPa) is dominated by the easterly wind with strong horizontal wind shear. We can also see at 200hPa level that the southeast wind is abruptly deflected west by the northeast wind.

Scenario B1 presents an intense mesoscale convective system at the 400hPa level (Figure 5c), but subsidence dominates at 300hPa levels. In the mesoscale convective system, Figure 5c of scenario B1 shows favorable conditions (LWC > 1 g/m3) for cumulonimbus clouds. However, the subsidence limits the cumulonimbus to expand vertically due to a strong northwesterly upper-level jet (ULJ). In this sense, the large-scale forcing played an important role in cumulus development during the model experiment. Indeed, in scenario B1, we have emphasized external forcing by increasing the number of model levels in the ABL, but the results are not consistent with the observation.

The scenario C presents the results of LES with one-way nesting from $D0_{i=4}$. This scenario has developed cumulonimbus with LWC $\geq$ 1 g/m^3 and has a spatial distribution of the LWC (Figure 5e) similar to the observed clouds (Figure 5a). Noted that this scenario presented the ABL water vapor relatively consistent with the observation. Scenario C predicted low and upper-level wind differently from scenario B. There is southeasterly wind at 400hPa level (Figure 5c), easterly wind at 300hPa level (Figure 5d), and northeasterly wind that predominates at the 200hPa level. This study assumes that the wind field in scenario C from 200 to 400hPa levels is more consistent with the observed than in scenario B because scenario C presented better clouds pattern than scenario B. Thus, the biased surface wind from scenario C discussed in section 3.1) did not influence the spatial distribution of the LWC. This is true when referring to the results from scenario B1, meaning that the internal forcing dominated the CC development during the model experiment at the Naqu site.

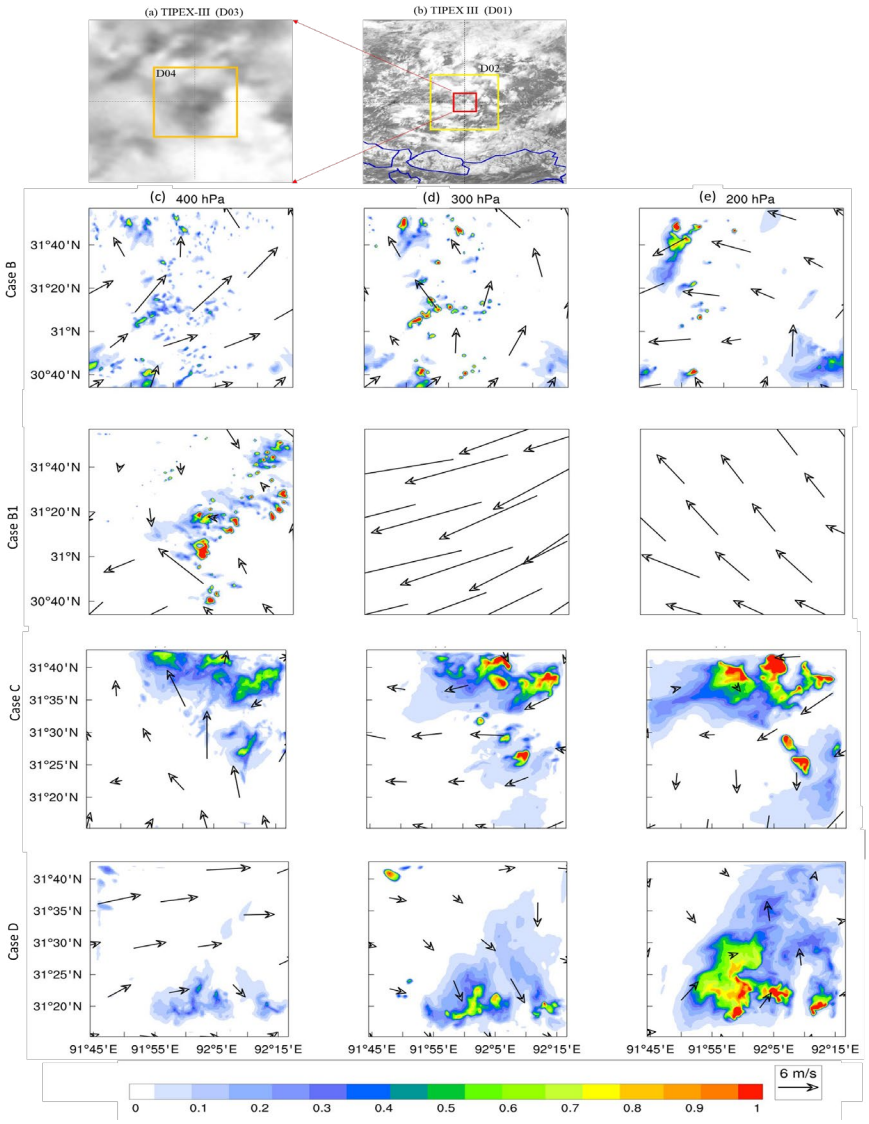

Figure 5: Liquid water content (LWC) and vertical wind shear at 16:48 local standard time (LST); vector field stands for wind direction and shaded represents LWC (g/m^3). Classification clouds types associated with the amount of LWC can be found in. Cases B and B1 from $D0_{i=3}$ =D 03, and C and D from $D0_{i=4}$ = D04 represent the scenarios in (c), (d) and (e) represent the columns of three panels.

The scenario D (Figures 5d and 5e), LES without a one-way nesting strategy presents cumulonimbus clouds from $D0_{i=4}$ with LWC ≥ 1 g/m^3. The atmosphere was quite turbulent due to pronounced wind shear. For example, the west wind at the 400hPa level (Figure 5d) changed to a north wind at the 300hPa level. By contrast, the wind at the 200hPa level (Figure 5e) has no specific direction. We note that scenario D has the best distribution of the water vapor mixing ratio in the ABL. When compared to scenarios B, B1, and C, scenario D was able to handle a complex orography. However, this scenario failed to reproduce the observed clouds.

4. Summary and Conclusions

We investigated the potential of the combined weather research and forecasting large-eddy simulation (WRF-LES) to simulate the development of cumulus clouds (CCs) over the south Tibetan plateau (STP) through atmospheric boundary-layer (ABL) processes. The objective was to use an observation nudging approach to ascertain the WRF-LES's optimal applicability for further experimental design. We carried out simulations of six scenarios with different setups and compared the results to observations from the third Tibetan Plateau Atmospheric Science Experiment (TIPEX-III), including Lidar ceilometer measurements, Fengyun 2D satellite images, radar reflectivity, sounding, and surface-base measurements such as temperature, wind, and heat fluxes. The new findings were obtained by applying observation nudging strategies and one-way nesting in two separate iterations.

We conducted a study involving six scenarios using mesoscale simulation in scenarios A, B, and B1, and large-eddy simulation (LES) in scenarios C, D, and E. Scenarios A and E were benchmark experiments to assess the effectiveness of observation nudging in scenarios B and D, respectively. Observation nudging was applied in scenarios B, B1, C, and D. Scenario B aimed to evaluate the impact of observational nudging on the simulation results, while scenario C sought to determine the effect of large-scale forcing on microscale circulation. Scenario C differed from scenario D only in the use of the one-way nesting strategy, while scenario D served as a control experiment to assess the effectiveness of the one-way nesting strategy used in scenario C. The model setting with observation nudging produced accurate results compared to the other scenarios. The field observations were inadequately captured in Scenarios A, B1, and E. Notably, scenario B1, which emphasized external forcing, exhibited inconsistent results with the observations. This highlights the important role of large-scale forcing in the development of cumulus clouds within a specific area during the model experiment. Upon comparing the simulated time series with the observed data, it was found that scenario B perfectly replicated the observed time series, albeit with low microphysical particles. Scenario D failed to replicate the microphysics patterns accurately but successfully recreated an ABL consistent with the observations. The scenario C had a relatively good representation of ABL and better reproduced the microphysical pattern, which also confirms the role of the large-scale forcing in cumulus development over Naqu during the model experiment. For simulating cumulus clouds, we recommend using scenarios B and C as they effectively capture the combined effects of ABL processes and cumulus cloud development observed during the model experiment. However, the WRF-LES model exhibited certain biases due to unreliable data, such as limited soundings taken only twice a day. Therefore, for scientific purposes and cloud simulation over Naqu, scenarios B and C can still be improved by focusing on the model's response to terrain and meteorological initial and boundary conditions. In the context of this model experiment, the high-resolution data from the Shuttle Radar Topography Mission did not produce satisfactory results, despite early hopes for an improvement.

It is important to statistically stabilize the model during the spin-up process, as the coupled WRF-LES model requires reliable mesoscale simulation data. As part of this study, a series of simulations were conducted by varying the spin-up time as preliminary work to determine the time interval that best matched the simulation. Based on these results, part B of this paper will discuss the development mechanism of deep cumulus convection over Naqu during the model experiment. Furthermore, this study will continue with the scenario using observation nudging in an improved setting and metrics for comparison to confirm the results of this simulation.

Funding

This work was supported by the Chinese academy of sciences (CAS), the world academy of sciences (TWAS) and substantially supported by the National Science and Technology Major Project of the Ministry of Science and Technology of China (2018YFC1505704).

Acknowledgment

The authors wish to express their sincere gratitude to their esteemed laboratory colleagues, Hu Wenhao and Zhang Tianyu, for their invaluable assistance in resolving complex technical challenges encountered during this project. Furthermore, they would like to extend their heartfelt appreciation to the Ministry of Higher Education of Togo, the National Meteorological Agency of Togo, the World Meteorological Organization, the Chinese Academy of Sciences, and the World Academy of Science for their unwavering support of the authors' advanced studies in various capacities.

References

1. Emanuel, K. A. (1997). Overview of atmospheric convection. In *The Physics and Parameterization of Moist Atmospheric Convection* (pp. 1-28). Dordrecht: Springer Netherlands.
2. Ravichandran, S., & Narasimha, R. (2020). Non-precipitating shallow cumulus clouds: theory and direct numerical simulation. *arXiv preprint arXiv:2004.09631.*
3. Kane, R. L., & Klein, D. E. (2005). Carbon sequestration. In *Advanced Air and Noise Pollution Control* (pp. 97-112). Totowa, NJ: Humana Press.
4. Krueger, S. K. (1988). Numerical simulation of tropical cumulus clouds and their interaction with the subcloud layer. *Journal of Atmospheric Sciences, 45*(16), 2221-2250.
5. Mechem, D. B., & Oberthaler, A. J. (2013). Numerical

simulation of tropical cumulus congestus during TOGA COARE. *Journal of Advances in Modeling Earth Systems, 5*(3), 623-637.
6. Ray, P. (Ed.). (2015). *Mesoscale meteorology and forecasting*. Springer.
7. Qiu, J. (2008). China: The third pole. *Nature, 454*(7203), 393-397.
8. Immerzeel, W. W., Van Beek, L. P., & Bierkens, M. F. (2010). Climate change will affect the Asian water towers. *science, 328*(5984), 1382-1385.
9. Li, Y., & Zhang, M. (2016). Cumulus over the Tibetan Plateau in the summer based on CloudSat–CALIPSO data. *Journal of Climate, 29*(3), 1219-1230.
10. Mukherji, A., Molden, D., Nepal, S., Rasul, G., & Wagnon, P. (2015). Himalayan waters at the crossroads: issues and challenges. *International Journal of Water Resources Development, 31*(2), 151-160.
11. Varis, O., Kummu, M., & Salmivaara, A. (2012). Ten major rivers in monsoon Asia-Pacific: An assessment of vulnerability. *Applied Geography, 32*(2), 441-454.
12. Zhao, P., Li, Y., Guo, X., Xu, X., Liu, Y., Tang, S., ... & Zhou, X. (2019). The Tibetan Plateau surface-atmosphere coupling system and its weather and climate effects: The Third Tibetan Plateau Atmospheric Science Experiment. *Journal of Meteorological Research, 33*, 375-399.
13. Fu, R., Hu, Y., Wright, J. S., Jiang, J. H., Dickinson, R. E., Chen, M., ... & Wu, D. L. (2006). Short circuit of water vapor and polluted air to the global stratosphere by convective transport over the Tibetan Plateau. *Proceedings of the National Academy of Sciences, 103*(15), 5664-5669.
14. Stocker, T. F., Qin, D., Plattner, G. K., Tignor, M. M., Allen, S. K., Boschung, J., ... & Midgley, P. M. (2014). Climate Change 2013: The physical science basis. contribution of working group I to the fifth assessment report of IPCC the intergovernmental panel on climate change.
15. Liu, Y., Liu, Y., Muñoz-Esparza, D., Hu, F., Yan, C., & Miao, S. (2020). Simulation of flow fields in complex terrain with WRF-LES: Sensitivity assessment of different PBL treatments. *Journal of Applied Meteorology and Climatology, 59*(9), 1481-1501.
16. Liu, L., Zheng, J., Ruan, Z., Cui, Z., Hu, Z., Wu, S., ... & Wu, Y. (2015). Comprehensive radar observations of clouds and precipitation over the Tibetan Plateau and preliminary analysis of cloud properties. *Journal of Meteorological Research, 29*(4), 546-561.
17. Zhao, P., Xu, X., Chen, F., Guo, X., Zheng, X., Liu, L., ... & Zhou, X. (2018). The third atmospheric scientific experiment for understanding the earth–atmosphere coupled system over the Tibetan Plateau and its effects. *Bulletin of the American Meteorological Society, 99*(4), 757-776.
18. Kpaikpai, B., Kpaikpai, B., Sun, J., Zhu, J., Huai, X., & Vuguziga, F. (2022). Mesoscale and Large-Eddy Simulation of the Boundary Layer Process of Cumulus Development over Naqu, Tibetan Plateau Part A: Comparison Between Simulation and Observation. *Authorea Preprints.*
19. Anthes, R. A. (1986). The general question of predictability. In *Mesoscale meteorology and forecasting* (pp. 636-656). Boston, MA: American Meteorological Society.
20. Emanuel, K. (Ed.). (2015). *The representation of cumulus convection in numerical models.* Springer.
21. Fujita, T. T. (1986). Mesoscale classifications: their history and their application to forecasting. In *Mesoscale meteorology and forecasting* (pp. 18-35). Boston, MA: American Meteorological Society.
22. Wang, T., Hu, C., Li, N., & Hou, Z. (2002). Numerical analysis of ground temperature in Qinghai-Tibet Plateau. *Science in China Series E: Technolgical Science, 45,* 433-443.
23. Wu, G., Liu, Y., Zhang, Q., Duan, A., Wang, T., Wan, R., ... & Liang, X. (2007). The influence of mechanical and thermal forcing by the Tibetan Plateau on Asian climate. *Journal of Hydrometeorology, 8*(4), 770-789.
24. Flohn, H. (1968). *Contributions to a meteorology of the Tibetan Highlands* (Vol. 130, p. 120). Fort Collins, Colo: Department of Atmospheric Science, Colorado State University.
25. Li, L., Yang, S., Wang, Z., Zhu, X., & Tang, H. (2010). Evidence of warming and wetting climate over the Qinghai-Tibet Plateau. *Arctic, Antarctic, and Alpine Research, 42*(4), 449-457.
26. Ding, J., Cuo, L., Zhang, Y., & Zhu, F. (2018). Monthly and annual temperature extremes and their changes on the Tibetan Plateau and its surroundings during 1963–2015. *Scientific reports, 8*(1), 11860.
27. Liu, X., Yin, Z. Y., Shao, X., & Qin, N. (2006). Temporal trends and variability of daily maximum and minimum, extreme temperature events, and growing season length over the eastern and central Tibetan Plateau during 1961–2003. *Journal of Geophysical Research: Atmospheres, 111*(D19).
28. Wang, J., Chen, X., Hu, Q., & Liu, J. (2020). Responses of terrestrial water storage to climate variation in the Tibetan Plateau. *Journal of hydrology, 584*, 124652.
29. Lei, Y., Shi, J., Xiong, C., & Ji, D. (2021). Tracking the atmospheric–terrestrial water cycle over the Tibetan Plateau based on ERA5 and grace. *Journal of Climate, 34*(15), 6459-6471.
30. Yang, K., Koike, T., Fujii, H., Tamura, T., Xu, X., Bian, L., & Zhou, M. (2004). The daytime evolution of the atmospheric boundary layer and convection over the Tibetan Plateau: observations and simulations. *Journal of the Meteorological Society of Japan. Ser. II, 82*(6), 1777-1792.
31. Ao, Y., Li, J., Li, Z., Lyu, S., Jiang, C., & Wang, M. (2017). Relation between the atmospheric boundary layer and impact factors under severe surface thermal conditions. *Advances in Meteorology, 2017.*
32. Chen, X., Anel, J. A., Su, Z., de la Torre, L., Kelder, H., van Peet, J., & Ma, Y. (2013). The deep atmospheric boundary layer and its significance to the stratosphere and troposphere exchange over the Tibetan Plateau. *PloS one, 8*(2), e56909.
33. Li, Y., & Gao, W. (2007). Atmospheric boundary layer circulation on the eastern edge of the Tibetan Plateau, China, in summer. *Arctic, Antarctic, and Alpine Research, 39*(4), 708-713.
34. Sato, T. (2009). Influences of subtropical jet and Tibetan Plateau on precipitation pattern in Asia: Insights from regional climate modeling. *Quaternary International,*

194(1-2), 148-158.
35. Yanai, M., & Li, C. (1994). Mechanism of heating and the boundary layer over the Tibetan Plateau. *Monthly Weather Review, 122*(2), 305-323.
36. Zhao, P., Xu, X., Chen, F., Guo, X., Zheng, X., Liu, L., ... & Zhou, X. (2018). The third atmospheric scientific experiment for understanding the earth–atmosphere coupled system over the Tibetan Plateau and its effects. *Bulletin of the American Meteorological Society, 99*(4), 757-776.
37. Chen, X., Škerlak, B., Rotach, M. W., Añel, J. A., Su, Z., Ma, Y., & Li, M. (2016). Reasons for the extremely high-ranging planetary boundary layer over the western Tibetan Plateau in winter. *Journal of the atmospheric sciences, 73*(5), 2021-2038.
38. Slättberg, N., & Chen, D. (2020, May). A long-term climatology of planetary boundary layer height over the Tibetan Plateau revealed by ERA5. In *EGU General Assembly Conference Abstracts* (p. 5517).
39. Betts, A. K., & Ball, J. H. (1994). Budget analysis of FIFE 1987 sonde data. *Journal of Geophysical Research: Atmospheres, 99*(D2), 3655-3666.
40. Margulis, S. A., & Entekhabi, D. (2004). Boundary-layer entrainment estimation through assimilation of radiosonde and micrometeorological data into a mixed-layer model. *Boundary-Layer Meteorology, 110*, 405-433.
41. Fu, Y., Ma, Y., Zhong, L., Yang, Y., Guo, X., Wang, C., ... & Wang, D. (2020). Land-surface processes and summer-cloud-precipitation characteristics in the Tibetan Plateau and their effects on downstream weather: a review and perspective. *National Science Review, 7*(3), 500-515.
42. Tingyang, D., & Reiter, E. R. (1990). Some characteristics of cumulus convection over the Tibetan Plateau. *Advances in atmospheric sciences, 7,* 87-97.
43. Luo, Y., Zhang, R., Qian, W., Luo, Z., & Hu, X. (2011). Intercomparison of deep convection over the Tibetan Plateau–Asian monsoon region and subtropical North America in boreal summer using CloudSat/CALIPSO data. *Journal of Climate, 24*(8), 2164-2177.
44. Couvreux, F., Guichard, F., Austin, P. H., & Chen, F. (2009). Nature of the mesoscale boundary layer height and water vapor variability observed 14 June 2002 during the IHOP_2002 campaign. *Monthly weather review, 137*(1), 414-432.
45. Gao, W., Sui, C. H., Fan, J., Hu, Z., & Zhong, L. (2016). A study of cloud microphysics and precipitation over the Tibetan Plateau by radar observations and cloud-resolving model simulations. *Journal of Geophysical Research: Atmospheres, 121*(22), 13-735.
46. Larson, K., Hartmann, D. L., & Klein, S. A. (1999). The role of clouds, water vapor, circulation, and boundary layer structure in the sensitivity of the tropical climate. *Journal of Climate, 12*(8), 2359-2374.
47. Zheng, D., Van der Velde, R., Su, Z., Wen, J., Booij, M. J., Hoekstra, A. Y., & Wang, X. (2015). Under-canopy turbulence and root water uptake of a T ibetan meadow ecosystem modeled by N oah-MP. *Water Resources Research, 51*(7), 5735-5755.
48. Chow, F. K., Street, R. L., Xue, M., & Ferziger, J. H. (2005). Explicit filtering and reconstruction turbulence modeling for large-eddy simulation of neutral boundary layer flow. *Journal of the atmospheric sciences, 62*(7), 2058-2077.
49. Takemi, T., & Rotunno, R. (2003). The effects of subgrid model mixing and numerical filtering in simulations of mesoscale cloud systems. *Monthly Weather Review, 131*(9), 2085-2101.
50. Zhu, P., Albrecht, B. A., Ghate, V. P., & Zhu, Z. (2010). Multiple-scale simulations of stratocumulus clouds. *Journal of Geophysical Research: Atmospheres, 115*(D23).
51. Aryee, J. N. A., Amekudzi, L. K., Preko, K., Atiah, W. A., & Danuor, S. K. (2020). Estimation of planetary boundary layer height from radiosonde profiles over West Africa during the AMMA field campaign: Intercomparison of different methods. *Scientific African, 7,* e00228.
52. Buck, A. L. (1981). New equations for computing vapor pressure and enhancement factor. *Journal of Applied Meteorology (1962-1982),* 1527-1532.
53. Braithwaite, R. J. (2009). Calculation of sensible-heat flux over a melting ice surface using simple climate data and daily measurements of ablation. *Annals of Glaciology, 50*(50), 9-15.
54. Castellví, F., & Gavilán, P. (2021). Estimation of the latent heat flux over irrigated short fescue grass for different fetches. *Atmosphere, 12*(3), 322.
55. Gavilán, P., & Berengena, J. (2007). Accuracy of the Bowen ratio-energy balance method for measuring latent heat flux in a semiarid advective environment. *Irrigation Science, 25,* 127-140.
56. Kim, M. S., & Kwon, B. H. (2019). Estimation of sensible heat flux and atmospheric boundary layer height using an unmanned aerial vehicle. *Atmosphere, 10*(7), 363.
57. Wang, J., & Bras, R. L. (1998). A new method for estimation of sensible heat flux from air temperature. *Water resources research, 34*(9), 2281-2288.
58. Verma, S. B., Baldocchi, D. D., Anderson, D. E., Matt, D. R., & Clement, R. J. (1986). Eddy fluxes of CO 2, water vapor, and sensible heat over a deciduous forest. *Boundary-Layer Meteorology, 36*, 71-91.
59. Pond, S., Fissel, D. B., & Paulson, C. A. (1974). A note on bulk aerodynamic coefficients for sensible heat and moisture fluxes. *Boundary-Layer Meteorology, 6*, 333-339.
60. Kotthaus, S., & Grimmond, C. S. B. (2018). Atmospheric boundary-layer characteristics from ceilometer measurements. Part 1: A new method to track mixed layer height and classify clouds. *Quarterly Journal of the Royal Meteorological Society, 144*(714), 1525-1538.
61. Sokół, P., Stachlewska, I. S., Ungureanu, I., & Stefan, S. (2014). Evaluation of the boundary layer morning transition using the CL-31 ceilometer signals. *Acta Geophysica, 62,* 367-380.
62. Powers, J. G., Klemp, J. B., Skamarock, W. C., Davis, C. A., Dudhia, J., Gill, D. O., ... & Duda, M. G. (2017). The weather research and forecasting model: Overview, system efforts, and future directions. *Bulletin of the American Meteorological Society, 98*(8), 1717-1737.
63. Skamarock, W. C., Klemp, J. B., Dudhia, J., Gill, D. O., Barker, D. M., Duda, M. G., ... & Powers, J. G. (2008). A

description of the advanced research WRF version 3. *NCAR technical note, 475*, 113.
64. Gentry, M. S., & Lackmann, G. M. (2010). Sensitivity of simulated tropical cyclone structure and intensity to horizontal resolution. *Monthly Weather Review, 138*(3), 688-704.
65. Canuto, V. M., & Cheng, Y. (1997). Determination of the Smagorinsky–Lilly constant CS. *Physics of Fluids, 9*(5), 1368-1378.
66. Liu, Y., Warner, T., Liu, Y., Vincent, C., Wu, W., Mahoney, B., ... & Boehnert, J. (2011). Simultaneous nested modeling from the synoptic scale to the LES scale for wind energy applications. *Journal of Wind Engineering and Industrial Aerodynamics, 99*(4), 308-319.
67. Dai, C., Wang, Q., Kalogiros, J. A., Lenschow, D. H., Gao, Z., & Zhou, M. (2014). Determining boundary-layer height from aircraft measurements. *Boundary-layer meteorology, 152,* 277-302.
68. Dudhia, J. (2014). A history of mesoscale model development. *Asia-Pacific Journal of Atmospheric Sciences, 50,* 121-131.
69. Talbot, C., Bou-Zeid, E., & Smith, J. (2012). Nested mesoscale large-eddy simulations with WRF: Performance in real test cases. *Journal of Hydrometeorology, 13*(5), 1421-1441.
70. Cheng, W. C., Kendall, D. R., Putti, M., & Yeh, W. W. G. (2009). A nudging data assimilation algorithm for the identification of groundwater pumping. *Water resources research, 45*(8).
71. Chow, F. K., & Street, R. L. (2009). Evaluation of turbulence closure models for large-eddy simulation over complex terrain: flow over Askervein Hill. *Journal of Applied Meteorology and Climatology, 48*(5), 1050-1065.
72. Mirocha, J. D., Lundquist, J. K., & Kosović, B. (2010). Implementation of a nonlinear subfilter turbulence stress model for large-eddy simulation in the Advanced Research WRF model. *Monthly Weather Review, 138*(11), 4212-4228.
73. Shin, H. H., & Dudhia, J. (2016). Evaluation of PBL parameterizations in WRF at subkilometer grid spacings: Turbulence statistics in the dry convective boundary layer. *Monthly Weather Review, 144*(3), 1161-1177.
74. Moeng, C. H., & Wyngaard, J. C. (1989). Evaluation of turbulent transport and dissipation closures in second-order modeling. *Journal of the Atmospheric Sciences, 46*(14), 2311-2330.
75. Soriano, C., Jorba, O., & Baldasano, J. M. (2004). One-way nesting versus two-way nesting: does it really make a difference?. In *Air pollution modeling and its application XV* (pp. 177-185). Boston, MA: Springer US.
76. Viswanadhapalli, Y., Srinivas, C. V., Ramakrishna, S. S., & Prasad, K. B. H. (2014). Impact of period and timescale of FDDA analysis nudging on the numerical simulation of tropical cyclones in the Bay of Bengal. *Natural Hazards, 74*(3), 2109-2128.
77. Reen, B. P., Dumais, R. E., & Passner, J. E. (2016). Mitigating excessive drying from the use of observations in mesoscale modeling. *Journal of Applied Meteorology and Climatology, 55*(2), 365-388.
78. Deardorff, J. W. (1980). Stratocumulus-capped mixed layers derived from a three-dimensional model. *Boundary-layer meteorology, 18,* 495-527.
79. Sertel, E., Robock, A., & Ormeci, C. (2010). Impacts of land cover data quality on regional climate simulations. *International Journal of Climatology, 30*(13), 1942-1953.
80. Niu, G. Y., Yang, Z. L., Mitchell, K. E., Chen, F., Ek, M. B., Barlage, M., ... & Xia, Y. (2011). The community Noah land surface model with multiparameterization options (Noah-MP): 1. Model description and evaluation with local-scale measurements. *Journal of Geophysical Research: Atmospheres, 116*(D12).
81. Yang, Z. L., Niu, G. Y., Mitchell, K. E., Chen, F., Ek, M. B., Barlage, M., ... & Xia, Y. (2011). The community Noah land surface model with multiparameterization options (Noah-MP): 2. Evaluation over global river basins. *Journal of Geophysical Research: Atmospheres, 116*(D12).
82. Chen, T. H., Henderson-Sellers, A., Milly, P. C. D., Pitman, A. J., Beljaars, A. C. M., Polcher, J., ... & Zeng, Q. (1997). Cabauw experimental results from the project for intercomparison of land-surface parameterization schemes. *Journal of Climate, 10*(6), 1194-1215.
83. Van den Hurk, B. J. J. M., & Holtslag, A. A. M. (1997). On the bulk parameterization of surface fluxes for various conditions and parameter ranges. *Boundary-Layer Meteorology, 82*(1), 119-133.
84. Jiménez, P. A., Dudhia, J., González-Rouco, J. F., Navarro, J., Montávez, J. P., & García-Bustamante, E. (2012). A revised scheme for the WRF surface layer formulation. *Monthly weather review, 140*(3), 898-918.
85. Janić, Z. I. (2001). Nonsingular implementation of the Mellor-Yamada level 2.5 scheme in the NCEP Meso model.
86. Iacono, M. J., Delamere, J. S., Mlawer, E. J., Shephard, M. W., Clough, S. A., & Collins, W. D. (2008). Radiative forcing by long-lived greenhouse gases: Calculations with the AER radiative transfer models. *Journal of Geophysical Research: Atmospheres, 113*(D13).
87. Mlawer, E. J., Taubman, S. J., Brown, P. D., Iacono, M. J., & Clough, S. A. (1997). Radiative transfer for inhomogeneous atmospheres: RRTM, a validated correlated-k model for the longwave. *Journal of Geophysical Research: Atmospheres, 102*(D14), 16663-16682.
88. Kain, J. S. (2004). The Kain–Fritsch convective parameterization: an update. *Journal of applied meteorology, 43*(1), 170-181.
89. Jeworrek, J., West, G., & Stull, R. (2019). Evaluation of cumulus and microphysics parameterizations in WRF across the convective gray zone. *Weather and Forecasting, 34*(4), 1097-1115.
90. Heinze, R., Moseley, C., Böske, L. N., Muppa, S. K., Maurer, V., Raasch, S., & Stevens, B. (2017). Evaluation of large-eddy simulations forced with mesoscale model output for a multi-week period during a measurement campaign. *Atmospheric Chemistry and Physics, 17*(11), 7083-7109.
91. Casati, B., Wilson, L. J., Stephenson, D. B., Nurmi, P., Ghelli, A., Pocernich, M., ... & Mason, S. (2008). Forecast verification: current status and future directions. *Meteorological Applications: A journal of forecasting,*

practical applications, training techniques and modelling, 15(1), 3-18.
92. Willmott, C. J., Ackleson, S. G., Davis, R. E., Feddema, J. J., Klink, K. M., Legates, D. R., ... & Rowe, C. M. (1985). Statistics for the evaluation and comparison of models. *Journal of Geophysical Research: Oceans, 90*(C5), 8995-9005.
93. Hess, M., Koepke, P., & Schult, I. (1998). Optical properties of aerosols and clouds: The software package OPAC. *Bulletin of the American meteorological society, 79*(5), 831-844.
94. Guoping, L., Tingyang, D., Jun, W., Yuanfa, G., Haginoya, S., Longxun, C., & Weiliang, L. (1996). Determination of the drag coefficient over the Tibetan Plateau. *Advances in Atmospheric Sciences, 13,* 511-518.
95. Zheng, D., Van der Velde, R., Su, Z., Wen, J., Wang, X., Booij, M. J., ... & Ek, M. B. (2016). Impacts of Noah model physics on catchment-scale runoff simulations. *Journal of Geophysical Research: Atmospheres, 121*(2), 807-832.